OPEN ACCESS



Rejuvenated Accretors Have Less Bound Envelopes: Impact of Roche Lobe Overflow on Subsequent Common Envelope Events

M. Renzo¹, E. Zapartas², S. Justham^{3,4,5}, K. Breivik¹, M. Lau^{1,6,7}, R. Farmer⁵, M. Cantiello¹, and B. D. Metzger^{1,8}, Center for Computational Astrophysics, Flatiron Institute, New York, NY 10010, USA; mrenzo@flatironinstitute.org

¹ I Center for Computational Astrophysics, Flatiron Institute, New York, NY 10010, USA; mrenzo@flatironinstitute.org

² IAASARS, National Observatory of Athens, Vas. Pavlou and I. Metaxa, Penteli, 15236, Greece

³ School of Astronomy and Space Science, University of the Chinese Academy of Sciences, Beijing 100012, People's Republic of China

⁴ Anton Pannekoek Institute of Astronomy and GRAPPA, University of Amsterdam, Science Park 904, 1098 XH Amsterdam, The Netherlands

⁵ Max-Planck-Institut für Astrophysik, Karl-Schwarzschild-Strae 1, D-85741 Garching, Germany

⁶ School of Physics and Astronomy, Monash University, Clayton, Victoria 3800, Australia

⁷ OzGrav: The ARC Centre of Excellence for Gravitational Wave Discovery, Victoria 3122, Australia

⁸ Columbia Astrophysics Laboratory, Columbia University, New York, NY 10027, USA

**Received 2022 June 30; revised 2022 November 14; accepted 2022 November 18; published 2023 January 11

Abstract

Common envelope (CE) evolution is an outstanding open problem in stellar evolution, critical to the formation of compact binaries including gravitational-wave sources. In the "classical" isolated binary evolution scenario for double compact objects, the CE is usually the second mass transfer phase. Thus, the donor star of the CE is the product of a previous binary interaction, often stable Roche lobe overflow (RLOF). Because of the accretion of mass during the first RLOF, the main-sequence core of the accretor star grows and is "rejuvenated." This modifies the core-envelope boundary region and decreases significantly the envelope binding energy for the remaining evolution. Comparing accretor stars from self-consistent binary models to stars evolved as single, we demonstrate that the rejuvenation can lower the energy required to eject a CE by \sim 42%–96% for both black hole and neutron star progenitors, depending on the evolutionary stage and final orbital separation. Therefore, binaries experiencing first stable mass transfer may more easily survive subsequent CE events and result in possibly wider final separations compared to current predictions. Despite their high mass, our accretors also experience extended "blue loops," which may have observational consequences for low-metallicity stellar populations and asteroseismology.

Unified Astronomy Thesaurus concepts: Binary stars (154); Common envelope binary stars (2156); Roche lobe overflow (2155)

1. Introduction

Common envelope (CE) evolution is important for massive isolated binaries to become gravitational-wave (GW) sources, despite recent debates on its relevance for the progenitors of the most massive binary black holes (e.g., Pavlovskii et al. 2017; van den Heuvel et al. 2017; Klencki et al. 2021, 2022; Marchant et al. 2021; van Son et al. 2022). CE remains a crucial step in the formation, among many other compact binaries, of cataclysmic variables (e.g., Paczynski 1976), double white dwarfs (e.g., Zorotovic et al. 2010), binary neutron stars (NSs, e.g., VignaGomez et al. 2018, 2020), merging black hole–neutron stars (e.g., Kruckow et al. 2018; Broekgaarden & Berger 2021), and possibly low-mass binary black holes (BHs, e.g., Dominik et al. 2012; van Son et al. 2022).

In the "classical scenario" for binary BHs and/or NSs (e.g., Tutukov & YungelSon 1993; Belczynski et al. 2016; Tauris et al. 2017), the progenitor binary experiences a first dynamically stable mass transfer through Roche lobe overflow (RLOF) between two noncompact stars. Subsequently, the initially more massive RLOF donor collapses to a compact object without disrupting the binary (e.g., Blaauw 1961; Renzo et al. 2019). Only afterwards, as the initially less massive RLOF accretor expands, a second masstransfer phase occurs and it can be dynamically unstable, which is

Original content from this work may be used under the terms of the Creative Commons Attribution 4.0 licence. Any further distribution of this work must maintain attribution to the author(s) and the title of the work, journal citation and DOI.

a CE (e.g., Dominik et al. 2012; Belczynski et al. 2016; Kruckow et al. 2018). This second mass transfer is responsible for the orbital shrinking (Paczynski 1976) allowing the system to merge within the age of the universe. Therefore, in this scenario, the donor star of the CE is the former accretor of the first RLOF (e.g., Klencki et al. 2021; Law-Smith et al. 2020; Renzo & Gotberg 2021).

The first stable RLOF typically occurs during the main sequence of the initially less massive star and accretion modifies its structure (e.g., Neo et al. 1977; Packet 1981; Blaauw 1993; Cantiello et al. 2007; Renzo & Gotberg 2021). On top of the enrichment of the envelope with CNO-processed material from the donor star core (Blaauw 1993; El-Badry et al. 2022), and the substantial spin-up (e.g., Packet 1981), accretors are expected to adjust their core size to the new mass in a "rejuvenation" process (e.g., Neo et al. 1977; Hellings 1983, 1984). The readjustment is driven by mixing at the boundary between the convective core and the envelope, which refuels the burning region of hydrogen (H), increasing the stellar lifetime. This mixing also affects the thermal structure of the partially H-depleted layer above the helium-rich core (He), which we refer to as a core-envelope boundary (CEB) region. It is in the CEB that the density rises and most of the envelope binding energy is accumulated for the remaining stellar lifetime (e.g., Tauris & Dewi 2001; Ivanova et al. 2013, 2020). Consequently, the success or failure of the CE ejection, and the final separation, are likely decided in the CEB layer and may be different depending on whether the CE-donor accreted mass previously or not.

Here, we use structure and evolution binary models to study the impact of the first RLOF phase on the outcome of possible subsequent CE events. Section 2 describes our MESA calculations. In Section 3 we show the ratio of binding energy of our accretor models divided by the binding energy of single stars with the same total post-RLOF mass. We discuss our findings and conclude in Section 4. Appendix A presents a proof-of-principle numerical experiment illustrating the effect of changing the CEB region and rotation on the envelope binding energy, and Appendices B–D present additional plots of our model grids. Appendix E explains how to reproduce our results.

2. Precommon Envelope Evolution

We use MESA (version 15140, Paxton et al. 2011, 2013, 2015, 2018, 2019; Jermyn et al. 2022) to compute the evolution of binaries that experience mass transfer after the end of the donor's main sequence, which is case B RLOF (Kippenhahn & Weigert 1967). Our output files are compatible for use in the population synthesis code POSYDON (Fragos et al. 2022) and publicly available together with our input files and customized routines at doi:10.5281/zenodo.7036016. Our setup is similar to Renzo & Gotberg (2021), except for the metallicity: here we adopt $Z = 0.0019 \simeq Z_{\odot}/10$, relevant for the progenitor population of GW events (e.g., van Son et al. 2022). Moreover, we apply throughout the star a small amount of mixing with diffusivity $min_D_mix=0.01 \text{ cm}^2 \text{ s}^{-1}$. This improves the numerical stability by smoothing properties across adjacent cells, without introducing significant quantitative variations, and is a typical numerical technique used in asteroseismology calculations (J. Fuller, private communication).

We adopt an initial period P=100 days and choose initial masses $(M_1, M_2)=(18, 15)$, (20, 17), (38, 30) M_{\odot} . We focus on the initially less massive stars, which after accretion become $M_2=15 \rightarrow 18$, $17 \rightarrow 20$, $30 \rightarrow 36$ M_{\odot} , roughly representative of NS progenitors, uncertain core-collapse outcome, and BH progenitors, respectively. However, the core-collapse outcomes (NS or BH formation, with explosion or not), cannot be decided solely based on the (total or core) mass of a star (e.g., O'Connor & Ott 2011; Farmer et al. 2016; Patton & Sukhbold 2020; Zapartas et al. 2021; Patton et al. 2022).

During the binary evolution, we account for tidal interactions assuming each stellar layer reacts on its own timescale (see Paxton et al. 2015). At mass transfer, our MESA models assume that the accretion efficiency is limited by rotationally enhanced wind mass loss (e.g., Sravan et al. 2019; Wang et al. 2020; Renzo & Gotberg 2021; Sen et al. 2022). However, this may lead to less conservative mass transfer than suggested by observations (e.g., Wang et al. 2021).

After the donor detaches from the Roche lobe, our simulations artificially separate ⁹ the stars and continue the evolution of the accretor as a single star until it reaches carbon depletion (defined by central carbon mass fraction $X_c(^{12}C) < 2 \times 10^{-4}$). Reducing the complexity by not simulating the late evolutionary phases of the RLOF donors saves significant computing time at a small price in accuracy of the RLOF accretors. Separating the stars, we neglect further possible, but not expected, mass-transfer episodes (case BB RLOF, Delgado & Thomas 1981; Laplace et al. 2020). We also neglect

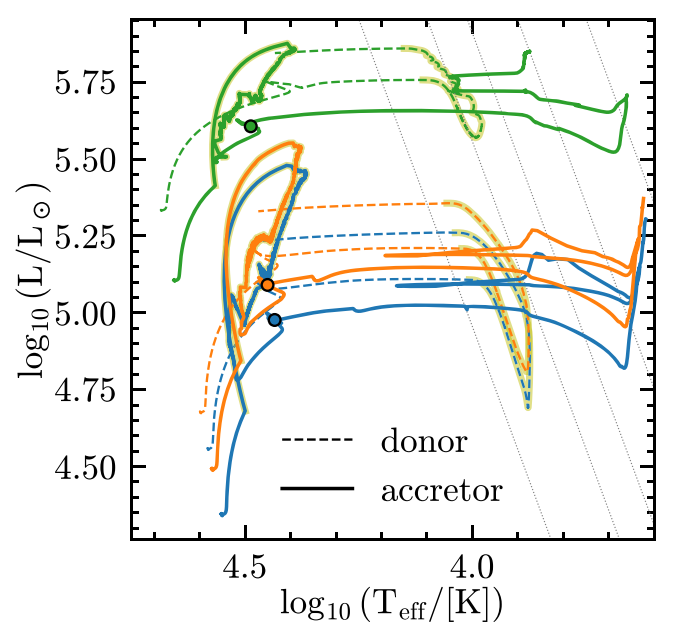


Figure 1. H-R diagram of the binary systems. The thin dashed lines show the evolution of the donors until RLOF detachment, the solid lines show the accretors from ZAMS, through RLOF (marked by a yellow outline), until core carbon depletion. Dots with black outlines mark the accretor's TAMS (not shown for donor). The thin dotted lines mark constant radii of $R=100,200,300,500,1000~R_{\odot}$; all models have Z=0.0019, an initial orbital period of $100~{\rm days}$, and initial masses of 38 and $30~M_{\odot}$ (green), 20 and $17~M_{\odot}$ (orange), $18~{\rm and}~15~M_{\odot}$ (blue).

post-RLOF tides, which are expected to be negligible for wide pre-CE binaries. Finally, we ignore the impact of the donor's supernova ejecta with the accretor (which has a small and short-lasting effect only on the outermost layers, e.g., Hirai et al. 2018; Ogata et al. 2021; R. Hirai, private communication) and the orbital consequences of the core-collapse (e.g., Brandt & Podsiadlowski 1995; Kalogera 1996; Tauris & Takens 1998; Renzo et al. 2019). To illustrate the physical reason why the first RLOF may influence the envelope structure of the accretor much later on, we also compute comparison stars. For each mass, we compute nonrotating single stars with an otherwise identical setup, and "engineered" stars that we modify at terminal age main sequence (TAMS, central hydrogen mass fraction $X_c(^1\text{H}) < 10^{-4}$) to mimic crudely the impact of rejuvenation of the accretor's CEB (see Appendix A).

At the onset of a CE event, the photospheric radius $R \equiv R_{\rm RL,donor}$ is the size of the Roche lobe of the donor star determined by the binary separation and mass ratio (e.g., Paczynski 1971; Eggleton 1983). Thus, we compare the internal structure of accretors to single and engineered stars at various epochs defined by a fixed photospheric radius $R = 100, 200, 300, 500, 1000 R_{\odot}$.

3. Accretors from Self-consistent Binary Models

Figure 1 shows the evolution of our binaries on the Hertzsprung–Russell (H-R) diagram. The thin dashed lines show the evolution of the donor stars (e.g., Morton 1960; Gotberg et al. 2018; Laplace et al. 2021) from zero-age main sequence (ZAMS), through RLOF, until our definition of detachment. The solid lines correspond to the full evolution of the accretors, from ZAMS, through RLOF, until carbon depletion. The yellow outline of the tracks highlights the RLOF mass transfer (see, e.g., Renzo & Gotberg 2021). During

We make the routine to separate a MESA binary on-the-fly publicly available https://github.com/MESAHub/mesa-contrib/.

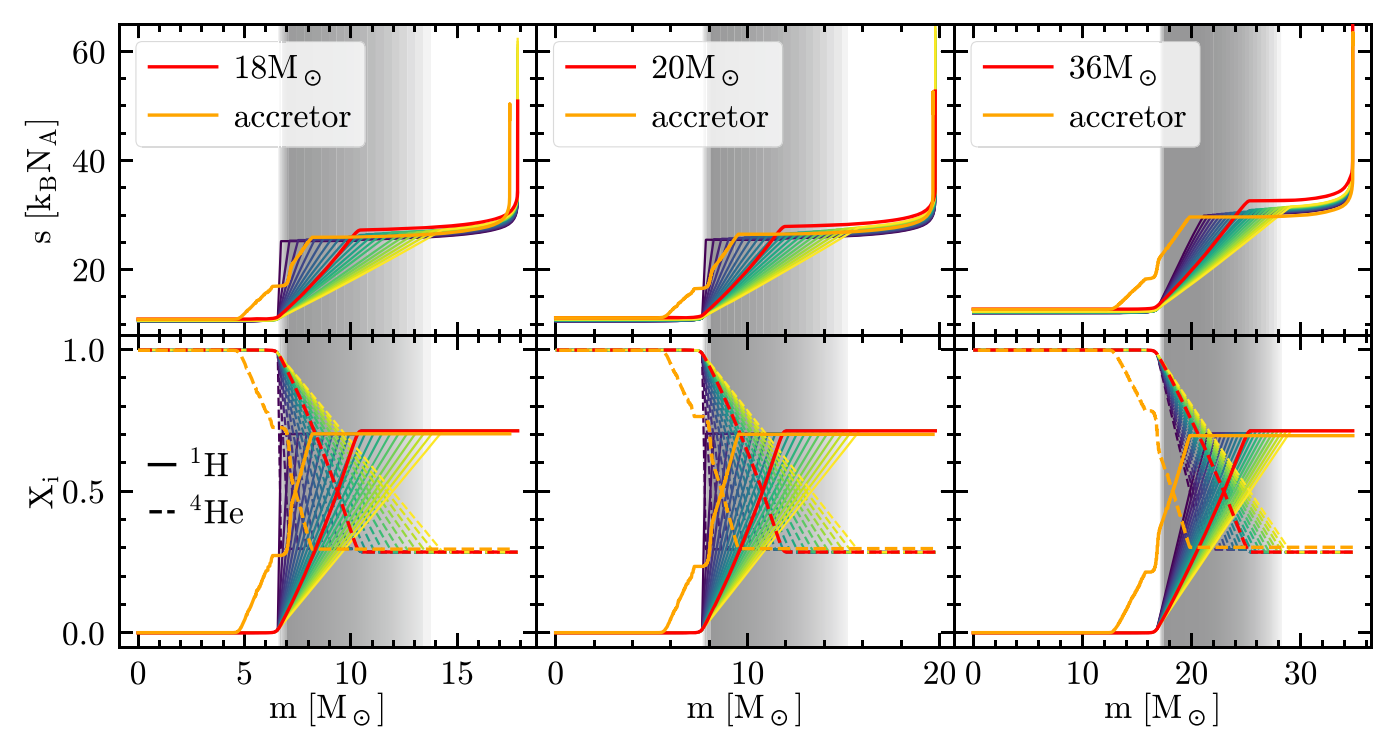


Figure 2. Specific entropy s (top row), H (bottom row, solid lines), and He (bottom row, dashed lines) TAMS profiles for nonrotating single stars (red), accretors (orange), and "engineered" models of the same total mass as the post-RLOF mass of the accretors. The overlapping gray bands emphasize the CEB region, $X_c(^1\text{H}) + 0.01 < X(^1\text{H}) < X_{\text{surf}}(^1\text{H}) - 0.01$, with X_c and X_{surf} the central and surface value of the hydrogen mass fraction. The CEB size of the engineered models increases from blue to yellow.

this phase the accretor progressively spins up, and accretes CNO-processed material from the donor's inner layers, which are mixed downwards in the envelope by meridional circulations and thermohaline mixing, and its core is rejuvenated because of the increased mass (see also Sravan et al. 2019; Renzo & Gotberg 2021; Wang et al. 2020). During the brief RLOF phase, our accretors grow to $M_2 = 15 \rightarrow 18$, $17 \rightarrow 20$, $30 \rightarrow 36 \, M_{\odot}$, respectively, corresponding to an overall mass transfer efficiency $\beta_{\text{RLOF}} = |\Delta M_{\text{accretor}}/\Delta M_{\text{donor}}| = 0.29, 0.30,$ and 0.43, respectively (see discussion in Renzo & Gotberg 2021). The binaries started with an initial separation of $\sim 300 \, R_{\odot}$ and widen to $\sim 380 \, R_{\odot}$ days by RLOF detachment. We expect further widening caused by the wind mass loss of both stars, allowing us to neglect tides in the remaining evolution and the impact of the RLOF-donor collapse (Hirai et al. 2018; Ogata et al. 2021).

All three accretor models experience a blueward evolution after beginning to ascend the Hayashi track. In the two lowest mass models, this results in a blue loop, which lasts $\sim\!10^5$ yr. These models spend a significant fraction of their He core burning as hot yellow/blue supergiants, and reach $\log_{10}(T_{\rm eff}/[{\rm K}])\gtrsim 4.2$. Our most massive accretor $(M_2=30\to36\,M_\odot)$ evolves toward hotter temperatures during core He burning, but never fully recovers closing the blue loop. Its excursion to hottest temperatures occurs after He core depletion and lasts $\sim\!10^4$ yr.

Blue loops are not expected for single stars with $M \gtrsim 12\,M_\odot$ (e.g., Walmswell et al. 2015), and their occurrence is known to be sensitive to the He profile above the H-burning shell, and specifically the mean molecular weight profile (Walmswell et al. 2015; Farrell et al. 2022). Thus it is not surprising that RLOF accretion, which modifies the CEB, may lead to blue loops, and formation of yellow supergiants. We note that

comparison single stars also experience late blueward evolution, but not a "loop" back to red. This behavior is likely related to the relatively high wind mass-loss rate assumed (see Renzo et al. 2017), and the models with initial mass $\gtrsim 30\,M_\odot$ are qualitatively similar to the most massive accretor in Figure 1 even without accreting matter from a companion: the occurrence of blue loops is notoriously sensitive to many single-star physics uncertainties, and while they appear consistently in our accretor models, their physicality should be tested further.

However, in the context of CE progenitors, blue loops are not crucial since they correspond to a decrease in radius, which would not result in binary interactions during the loop. They might change the mass-loss history of the accretor, but since they occur in a short evolutionary phase, their impact should be limited.

Figure 2 shows the specific entropy (s) profile—which determines the instantaneous dynamical response of the gas—and the H and He mass fractions at TAMS for our accretor models (orange), single nonrotating stars (red), and "engineered" models of roughly same total mass as the accretor post-RLOF. A gray region highlights the CEB, and their overlap produces the shade in Figure 2. We compare our models at the same total post-RLOF mass ($M \simeq M_2$) because it enters in Equation (1) and is typically used in rapid population synthesis codes to construct accretors from single-star models (e.g., Hurley et al. 2002; Breivik et al. 2020). We present in Figure 10 a comparison between TAMS profiles of accretors, single stars, and engineered models with the same *initial* mass as an alternative comparison that should bracket the range of sensible comparison models.

Because of the timing and duration of RLOF, accretion affects the CEB layers in more subtle ways than we impose in

our "engineered" models. One expects the CEB in accretors to be steeper than in a star evolving as single, resulting in models qualitatively more similar to our engineered models with the steeper entropy and composition in the CEB (darker lines in Figures 2–3, Figure 6, and Figures 10–11). The convective core of the accretor post-RLOF would naturally become more massive in a star with homogeneous composition. However, the He-enriched CEB can impede or prevent the growth of the core (e.g., Yoon & Langer 2005). The He enrichment increases with the stellar age, and thus with the duration of the pre-RLOF evolution. This duration depends on the binary architecture: for our binaries with initial P = 100 days and $q = M_2/M_1 \simeq 0.8$, RLOF starts after \sim 10, 9, and 5 Myr from the least massive to the most massive system, which correspond to central H mass fractions $X_c(^1H) = 0.27$, 0.23, and 0.21 for the accretors (see height of the plateaus in the orange lines in Figure 2). Our oversimplified engineered models do not exhibit such a plateau because they are constructed assuming instantaneous rejuvenation at TAMS (see Appendix A.1).

To quantify the impact of the first RLOF phase on the outcome of the second mass transfer phase, we evolve forward all the TAMS profiles shown in Figure 2 and compare them at fixed outer radii. In the "classical" binary evolution path, after the RLOF donor collapses to a compact object, the evolutionary expansion of the RLOF accretor triggers a CE. This phase of evolution is a complicated physics problem, not necessarily well described as an energetically closed system (e.g., Ivanova et al. 2013, 2020; Renzo et al. 2021). However, a common oversimplification is to assume energy conservation (" $\alpha_{CE}\lambda_{CE}$ algorithm," e.g., Webbink 1984; de Kool 1990; De Marco et al. 2011) to determine CE ejection and final separation. Here we focus on the RLOF-accretor/CE-donor binding energy profile as an indication for the ease of CE ejection. Even if imperfect, following common practice, we adopt this quantity as a proxy for the physical processes that determine the CE outcome and that allows us to compare models to each other. We calculate the cumulative binding energy (BE) outside mass coordinate m as (e.g., de Kool 1990; Dewi & Tauris 2000; Lau et al. 2022a):

$$BE(m, \alpha_{th}) = -\int_{m}^{M} dm' \left(-\frac{Gm'}{r(m')} + \alpha_{th} u(m') \right), \qquad (1)$$

with r(m') radius, u(m') the internal energy of a shell of mass thickness dm' and outer Lagrangian mass coordinate m', and Gthe gravitational constant. The integral goes from mass coordinate m, which can be thought of as the mass of the "core" surviving a hypothetical CE, to the surface. The parameter $0 \le \alpha_{th} \le 1$ is the fraction of internal energy (including recombination energy) that can be used to lift the shared CE (e.g., Han et al. 1995). It is possible that α_{th} may not be constant during a CE (e.g., if recombination happens in already unbound material it cannot contribute to the CE energetics, Lau et al. 2022b) or across binary systems entering a CE at different evolutionary stages. For $\alpha_{th} = 0$, Equation (1) gives the gravitational binding energy (dashed lines in Figures 6–7), while $\alpha_{th} = 1$ assumes perfectly fine-tuned use of all the internal energy (solid lines, see also Klencki et al. 2021). These two cases bracket the range of possible use of internal energy to eject the CE. The additional inclusion of a rotational-energy term $0.5\mathcal{I}\omega^2$ (with $\mathcal{I}=2r^2/3$ the specific moment of inertia) in the integral in Equation (1) contributes to

less than $\lesssim 10\%$ of the cumulative binding energy only in the outermost layers, likely to be crossed during a dynamical plungein in CE evolution, and only for $R \lesssim 300 \, R_{\odot}$; afterwards, even the accretor spins down significantly (see also Appendix A.2).

Because of the large range of BE across the stellar structures, it is hard to appreciate directly the magnitude of the effect of RLOF-driven rejuvenation on the BE profile (shown in Figure 9). Figure 3 presents the ratio of the local value of the cumulative binding energy from the surface of our accretor models divided by the comparison single stars, as a function of radius. The two lowest mass accretors (left and central column) do not expand to $R = 1000 \, R_\odot$ before carbon depletion. To compute the ratio, we interpolate linearly the single-star models on the mesh of our accretor, using the fractional Lagrangian mass coordinate m/M as independent coordinate. We calculate these ratios when both the stars reach for the first time radii R = 100, 200, 300, 500, $1000 \, R_\odot$ (see vertical gray dotted lines), corresponding to the assumed Roche lobe radius of the donor at the onset of the CE.

In each panel, radial coordinates r for which the lines in Figure 3 are below one correspond to radii at which the accretor models are less bound than the comparison single-star or engineered model. For $R \lesssim 300~R_{\odot}$, the outermost layers (more likely to be crossed by the binary during the dynamical plunge-in phase of the CE) may be slightly less bound in single stars than accretors (red line greater than 1)—partly because of the impact of rotation. But for most of the envelope radius, the ratio is smaller than one, suggesting it would take less energy to eject the outer layers of the envelope of the accretors down to such r. All of our accretor models, regardless of them being NS or BH progenitors, and regardless of their evolutionary phase, are qualitatively more similar to the darker lines representing engineered models with steeper CEB profiles.

The minimum ratio of binding energies occurs roughly at the inner edge of the CEB layer in Figure 3. Considering the ratio to single stars (red lines), the minima range between 0.56 and 0.07, 0.58 and 0.08, and 0.51 and 0.04 from our least to most massive binary. In other words, at the radius where the difference between accretors and single stars models is largest, which is also the location where the outcome of a common envelope is likely to be decided, the accretor's binding energy is roughly between ~ 50 – few percent of the binding energy of a single star. Regardless of the mass, the larger the outer radius the smaller the minimum of the ratio of binding energies: the differences caused by RLOF accretion and rejuvenation of the core grows as stars evolve and their core contracts.

Defining the He core boundary as the outermost location where X < 0.01 and Y > 0.1, we can fix $m = M_{\text{He}}$ in Equation (1) to obtain an integrated binding energy for the envelope:

$$BE_{env} \equiv BE(m = M_{He}, \alpha_{th} = 1).$$
 (2)

Figure 4 shows the evolution of this integrated envelope binding energy as a function of the outer radius. Each panel shows one of our binaries, from top to bottom: $36 + 30 \, M_{\odot}$, $20 + 17 \, M_{\odot}$, $18 + 15 \, M_{\odot}$. For each binary, the lower panel shows the ratios of the envelope binding energy of the accretor divided by the binding energy of the comparison single star (i.e., the ratio of the solid lines to the dotted lines in the panel above). To compute these ratios, we interpolate our accretor models on the time grid of the single stars using the central temperature $\log_{10}(T_c/[K])$ as an independent coordinate.

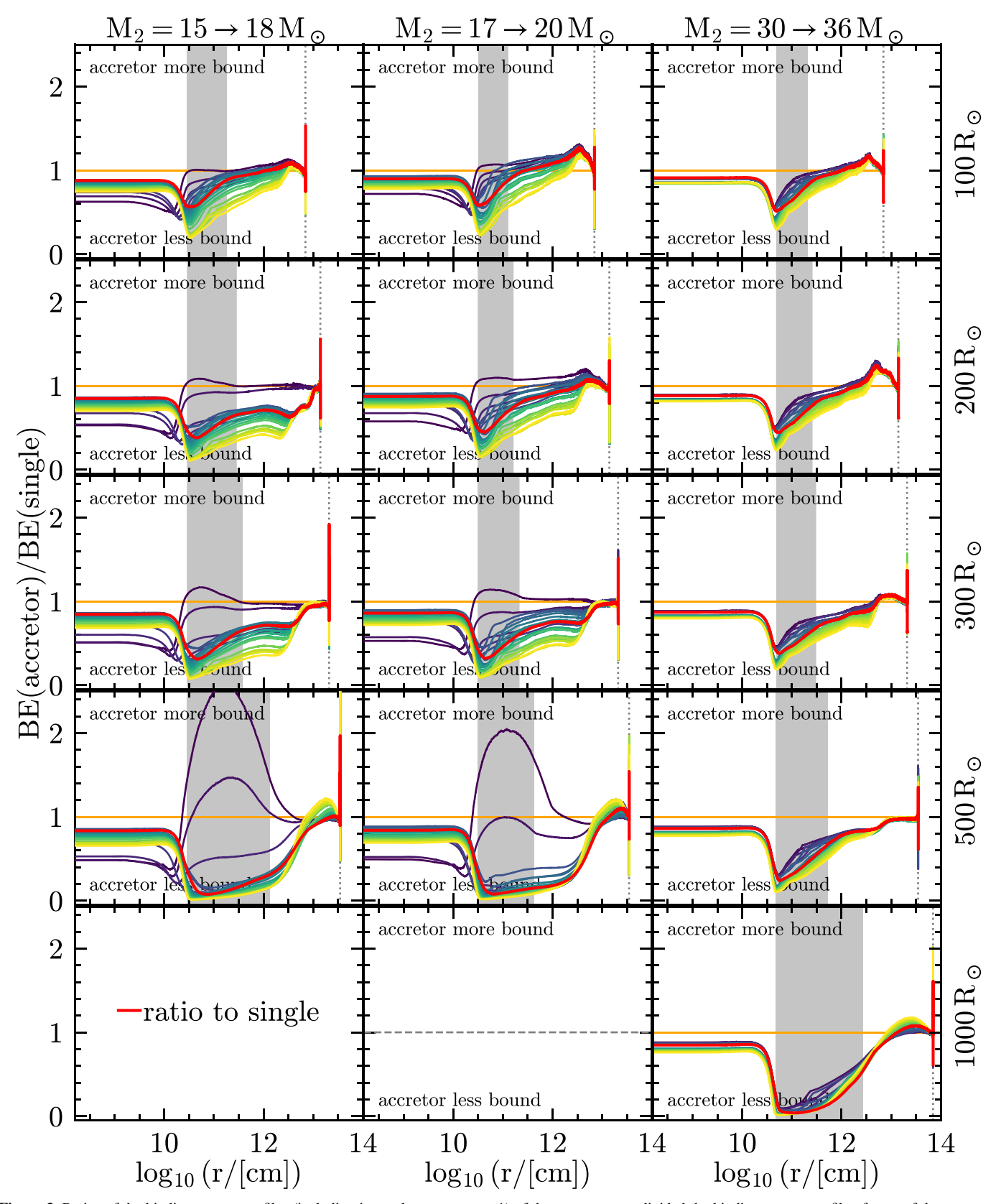


Figure 3. Ratios of the binding energy profiles (including internal energy, $\alpha_{th} = 1$) of the accretor stars divided the binding energy profile of stars of the same total mass post-RLOF. The orange solid line at 1 shows the ratio of the accretor to itself as a check on the models interpolation; red solid lines show the ratio of the accretor to a nonrotating single star, while the other colors show the ratio to "engineered" stars (see Figure 2, increasing CEB size from blue to yellow; see also Appendix A.1). Each panel shows the ratios at the first time the models reach the radius indicated on the right and by the vertical dotted gray lines. The vertical gray bands mark the radial extent of the CEB in the accretors only, which may differ in the other stars. For the binding energy profiles in the numerator and denominator of the fractions plotted here see Figure 9.

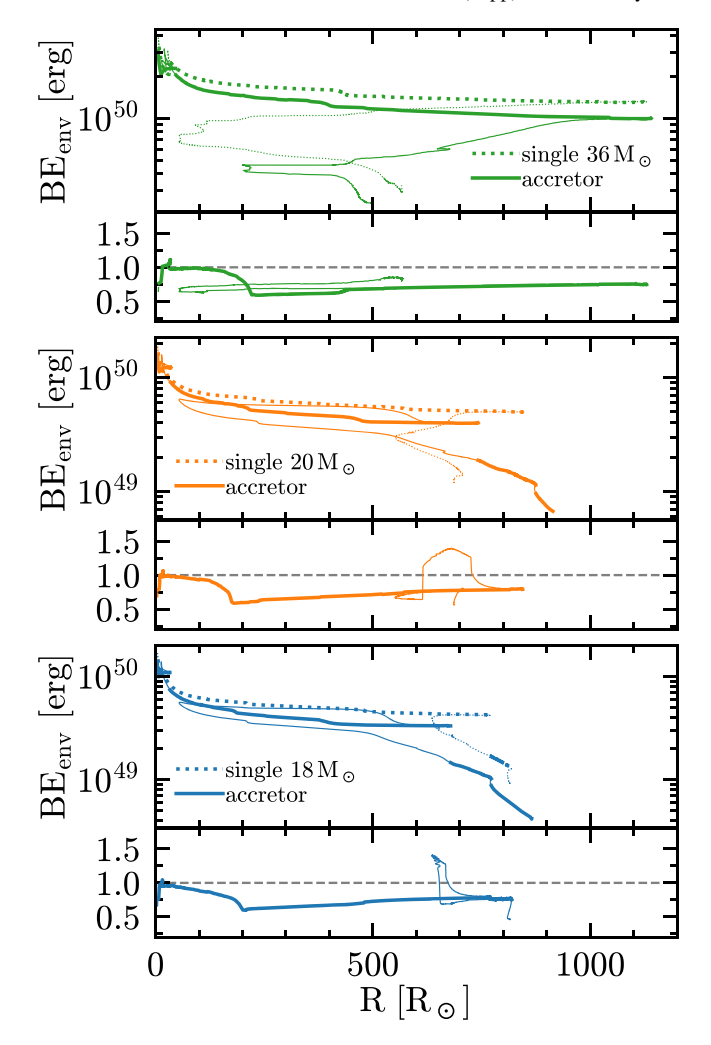


Figure 4. Evolution as a function of the photospheric radius R of the binding energy (including the thermal energy, $\alpha_{\rm th}=1$) of the accretors and single stars of the same (post-RLOF) total mass. The solid and dotted lines show the accretors and single stars, respectively, and they are thin when previously the models reached larger radii. The bottom panels show the ratio of the binding energies, which is always smaller than 1 the first time a certain radius R is reached (thick lines), indicating that the accretors might have envelopes easier to unbind in at the start of a CE event. Excursions above 1 of the ratio occur only during phases of radius decrease (thin lines), which could not initiate a CE. See Figure 4 for the radial binding energy profile at given outer radii R.

In each of the lower panels the ratios are lower than one (marked by the gray dashed lines) suggesting that post-RLOF accretor stars have envelopes that require less energy to be ejected in a CE event. The only times the binding energy of the accretor is higher than the corresponding single stars is during the blueward evolution discussed earlier, which would not trigger a CE.

4. Discussion and Conclusions

We have modeled the impact of mass transfer on the envelope structure of the accretor, focusing on the thermal timescale, post-donor-main-sequence case B RLOF (see Figure 1). The accretion of mass drives the growth of the accretor's core, changing the core/envelope boundary region and "rejuvenating" the star (Figure 2). As the accretors evolve beyond the main sequence, they experience large blue loops,

which are not expected in single stars of the same mass—with potential implications for asteroseismology (e.g., DornWallenstein et al. 2020), and the search for noninteracting companions to compact objects (e.g., Breivik et al. 2017; Andrews et al. 2019; Chawla et al. 2022).

The rejuvenation is driven by convective core boundary mixing (e.g., Hellings 1983, 1984; Cantiello et al. 2007; Renzo & Gotberg 2021), and does not occur in its absence (Braun & Langer 1995). The hydrodynamics of convective boundaries in a stellar regime is an active topic of research (e.g., Anders et al. 2022a, 2022b), and observations of the width of the main sequence (e.g., Brott et al. 2011) and asteroseismology (e.g., Moravveji et al. 2016) suggest the presence of convective boundary mixing in the core of massive main-sequence stars. In our one-dimensional accretor models, the dominant core boundary mixing is overshooting, with rotationally driven instabilities contributing to a lesser extent during late RLOF. We adopt an exponentially decreasing overshooting diffusion coefficient (Claret & Torres 2017), which may underestimate the amount of mixing at the accretor core boundary. After RLOF, a thick convective shell develops above the core (see Renzo & Gotberg 2021), which also contributes to the different binding energy profiles (see Figure 9).

We have focused on the structural consequences of RLOF accretion, specifically their impact on the subsequent binary interaction in the "classical" scenario to a GW merger: the CE event initiated by the RLOF accretor. Accretors have an overall lower binding energy of the envelope (both integrated from the surface to the He core; see Figure 4, and as a function of radius; see Figures 3, 9, and 11). The systematically lower binding energy of our accretor models compared to single stars of the same outer radius and total mass may imply easier to eject (post-RLOF, second) CE and wider post-CE separations.

Before the onset of the dynamical instability in a CE event, a pre-CE thermal timescale phase of mass transfer may occur (e.g., Hjellming & Webbnik 1987; Nandez et al. 2014; Pejcha et al. 2017; Blagorodnova 2021). This phase may impact the envelope structure of CE donors (through tidal interactions and mass loss) whether they are RLOF accretors (as in our models) or not. Multidimensional studies are needed to assess whether rejuvenation, rotation, tides, and the impact of the companion's supernova shock on accretor stars counteract or compound each other.

A key uncertainty in the CE outcome is the location of the separation between the (possibly) ejected envelope and the remaining core (e.g., Tauris & Dewi 2001). This affects equally each CE donor and can have an amplitude comparable to the effect of rejuvenation in accretors (see Figure 9 for three possible definition of "core"). In the case of rejuvenated CE donors, uncertainties in the core definition compound with the effect of rejuvenation itself.

Not all binary architectures necessarily result in rejuvenated accretors like the ones described here. Very massive BH progenitors ($M_{\rm ZAMS} \gtrsim 40\,M_{\odot}$) may not expand as red supergiants at all or avoid unstable mass transfer (e.g., Marchant et al. 2021; van Son et al. 2022). Since their main-sequence lifetimes are roughly independent of mass ($\sim 2.5-3$ Myr), at the first RLOF, accretors this massive may already have a deep core/envelope chemical gradient to prevent rejuvenation. However, more massive stars are generally easier to mix (including reaching rotationally induced chemically homogeneous evolution, e.g., Yoon & Langer 2005; de Mink &

Mandel 2016). Shorter initial periods (i.e., earlier mass transfer) and smaller radii during the binary interactions can prevent the red supergiant phase even at lower masses (Cantiello et al. 2007).

We have focused on accretor models for progenitors of NSs and BHs. However, the physical processes described should be similar in all accretor stars with convective main-sequence cores, down to initial mass $M_{\rm ZAMS} \gtrsim 1.2\,M_{\odot}$ (see also Wang et al. 2020). Thus, also a fraction of progenitors of binaries with white dwarfs, if sufficiently massive and experiencing a (case B) RLOF phase of evolution, may be influenced by the structural differences between single stars and RLOF accretors.

Including the structural reaction to accretion during RLOF in population synthesis simulations could impact the distribution of post-CE orbital separations, the predicted number of "reverse" stellar mergers (e.g., Zapartas et al. 2017), and the rate of GW mergers. Our grid consists only of three binaries, but could be extended to inform semianalytic approximations of the binding energy of CE donors that have accreted mass in a previous stable mass transfer phase (see also Figure 11).

We are grateful to Y. Götberg for invaluable discussions on binary physics, R. Luger for the development of **show your work!**, and to the POSYDON team for sharing their MESA setup. E.Z. acknowledges funding support from the European Research Council (ERC) under the European Union's Horizon 2020 research and innovation program (grant agreement No. 772086). S.J. acknowledges funding via the NWO Vidi research program BinWaves (project 639.042.728, PI: de Mink). Software: MESA Paxton et al. (2011, 2013, 2015, 2018), Jermyn et al. (2022) pyMESA (Farmer & Bauer 2018), POSYDON (Fragos et al. 2022), compare_workdir_MESA¹⁰, Ipython (Perez & Granger 2007), numpy (van der Walt et al. 2011), scipy (Virtanen et al. 2020), matplotlib (Hunter 2007), show your work! (Luger et al. 2021).

Appendix A Impact of Core-envelope Boundary and Rotation on the Binding Energy Profile

In this appendix, we introduce our "engineered" models and illustrate with examples how the envelope binding energy depends on the CEB region (Section A.1) and on the initial rotation rate of the star (Section A.2). Both can be significantly modified by accretion during the first RLOF.

Figure 5 shows an example grid of "engineered stars" of $20\,M_\odot$, similar to Figure 2. Starting from a nonrotating single star at TAMS (e.g., red model in Figure 5), we modify the CEB specific entropy (s), which controls the thermal properties of the gas, and its H, and He profiles—but do not change the mass fractions of other elements. Specifically, we keep the same inner and outer profiles, but impose a linear connection from the outer boundary of the H-depleted core to a mass coordinate, which we specify as a parameter (see Figure 5 and Figure 2). We let MESA relax the TAMS profiles to the desired entropy and composition profiles and then recover gravothermal and hydrostatic equilibrium, and then evolve until either carbon depletion or when the photospheric radius of these models first exceeds $1000\,R_\odot$.

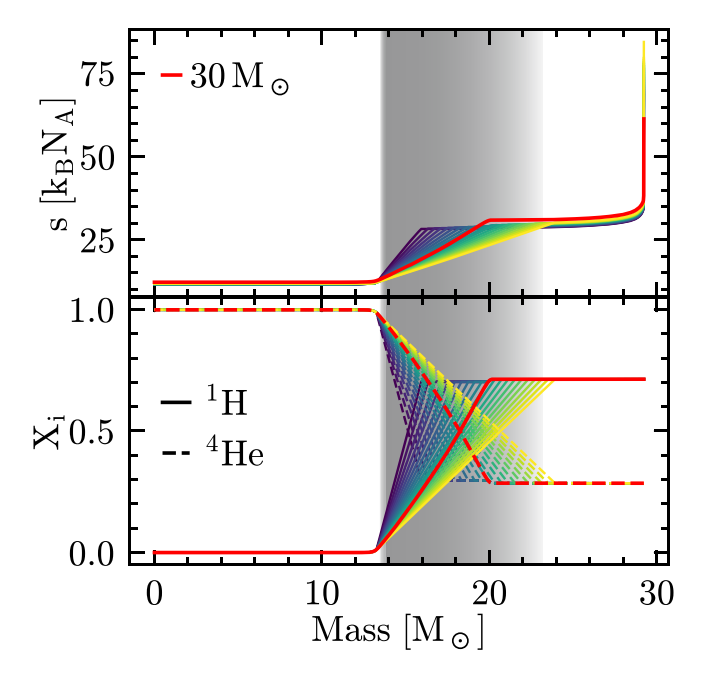


Figure 5. TAMS entropy profile of a single $30\,M_\odot$ star (red) and engineered models where we artificially modify the CEB region (gray shaded area partially overlapping for multiple models, increasing CEB size from blue to yellow). The CEB for a single $30\,M_\odot$ star has a mass thickness of $5.81\,M_\odot$ at TAMS, while the engineered models span the range $\sim 3-9.4\,M_\odot$.

A.1. Steepness of the Core-envelope Boundary

Figure 6 shows a comparison of the gravitational and binding energy profiles of a $30\,M_\odot$ single-star (red solid line) to "engineered" models, when stars first reach radius $R=500\,R_\odot$. Figure 6 shows that binding energy depends on the structure of the CEB region. In single stars, the CEB is determined by the extent of the convective boundary mixing and the recession in mass coordinate of the convective core. In Figure 6, lines of different colors show a trend with shallower entropy and composition profiles at TAMS (lighter curves in Figure 5) evolving into more bound inner envelopes (larger binding energy inside $\log_{10}(r/\text{cm}) \lesssim 11.5$), and vice versa.

A.2. Rotation

Mass transfer through RLOF also spins up the accreting star, often to critical rotation¹¹ (e.g., Lubow & Shu 1975; Packet 1981; Cantiello et al. 2007; Renzo & Gotberg 2021). To illustrate the impact of rotation, it is worth considering the CEB region and envelope structure of single-star models rotating since birth, although spinning up a star late during its main-sequence evolution has different structural consequences than natal rotation (see Renzo & Gotberg 2021).

Rotation has two main evolutionary effects: (i) mixing can change the core size directly (see Heger et al. 2000; Maeder & Meynet 2000); (ii) by inflating the equatorial region, rotation changes the temperature and opacity structure, and therefore the line driving of the wind (e.g., Muller & Vink 2014; Gagnier et al. 2019), affecting the rate of recession of the convective core (e.g., Renzo et al. 2017, 2020). Moreover, rotation can have a dynamical effect, resulting in mass loss through the combination

¹⁰ https://github.com/mathren/compare_workdir_MESA/releases/tag/2.0

 $[\]overline{^{11}}$ At critical rotation, the centrifugal force balances the gravitational pull at the equator, corresponding to critical angular frequency $\omega_{\rm crit} = \sqrt{(1-L/L_{\rm Edd})GM/R^3}$, with $L_{\rm Edd}$ the Eddington luminosity, and L the stellar luminosity.

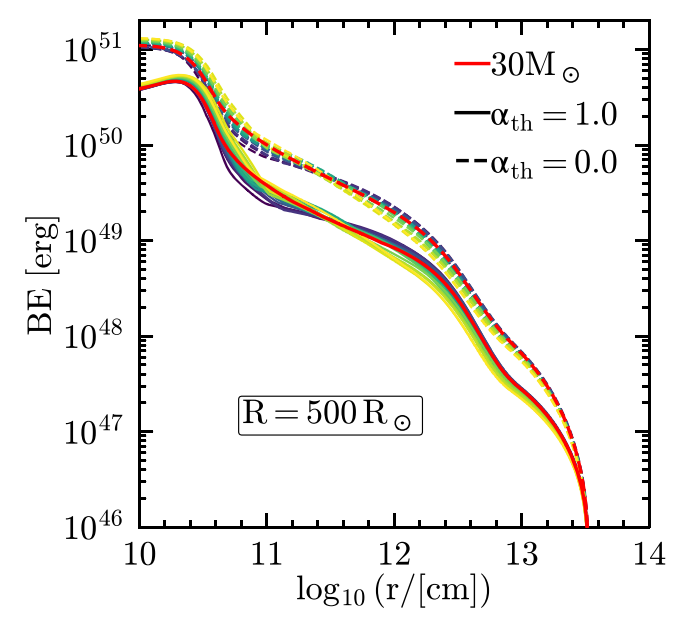


Figure 6. The structure of the CEB at the end of the main sequence impacts the envelope binding energy profile throughout the remaining evolution. Dashed lines show the gravitational contribution only; while solid lines include the contribution of the internal energy. The red lines show a $30\,M_\odot$, nonrotating, Z=0.0019 model compared to "engineered" models of the same mass (see Figure 5, increasing CEB size from blue to yellow), but artificially imposed profile at TAMS (other colors; see text). The top (bottom) axis indicates mass coordinate (radius). We compare the models when they first reach $500\,R_\odot$.

of centrifugal forces and radiative pressure ($\Gamma-\Omega$ limit, Langer 1998). One-dimensional stellar evolution codes commonly assume that rotation increases the total mass-loss rate (e.g., Langer 1998; Heger et al. 2000) though this may not always be true throughout the evolution (e.g., Gagnier et al.2019).

Figure 7 shows the gravitational binding energy profile of the single, nonrotating $18\,M_\odot$ star, compared to single stars of the same mass and varying initial $\omega/\omega_{\rm crit}$. For $\omega/\omega_{\rm crit}\lesssim 0.5$, corresponding to a generous upper bound for the typical birth rotation rate of single massive stars (e.g., RamirezAgudelo et al. 2015), the effect is modest but nonnegligible. For more extreme initial rotation rates (achievable during RLOF), the ratio of the He core mass to total mass is significantly changed by rotational mixing, which can result in larger binding energy differences than changing the CEB region at fixed core mass.

Figure 8 shows the ratio of the binding energy (see Figure 3) of a reference model divided the binding energy of the rotating models of Figure 7. The left column uses as a reference model for the numerator the nonrotating single $18 M_{\odot}$, while the right column uses our $15 \rightarrow 18 \, M_{\odot}$ accretor. The ordering of colors shows that the faster the initial rotation, the larger its structural effect on the star. However, single-star models, regardless of their initial rotation rate, are more similar to each other than any single rotating star is to the accretor: in each row, the ratios in the left column are closer to one than the ration in the right column. Moreover, the binding energy profiles of fast-rotating models (yellow) differ more than slow- and nonrotating models (blue and cyan) when compared to our accretor (i.e., their ratios are farther from one). Therefore, we do not recommend the use of fast-rotating single stars to mimic the effect of mass accretion and rejuvenation.

For stars accreting through RLOF in a binary both effects illustrated in Figure 6 and Figure 7 act simultaneously,

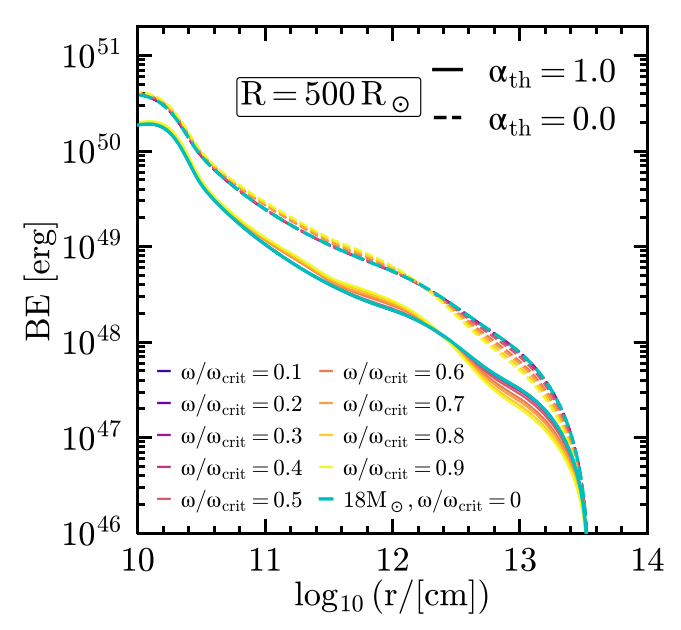


Figure 7. Same as Figure 6 but comparing single stars differing by their initial rotation rate.

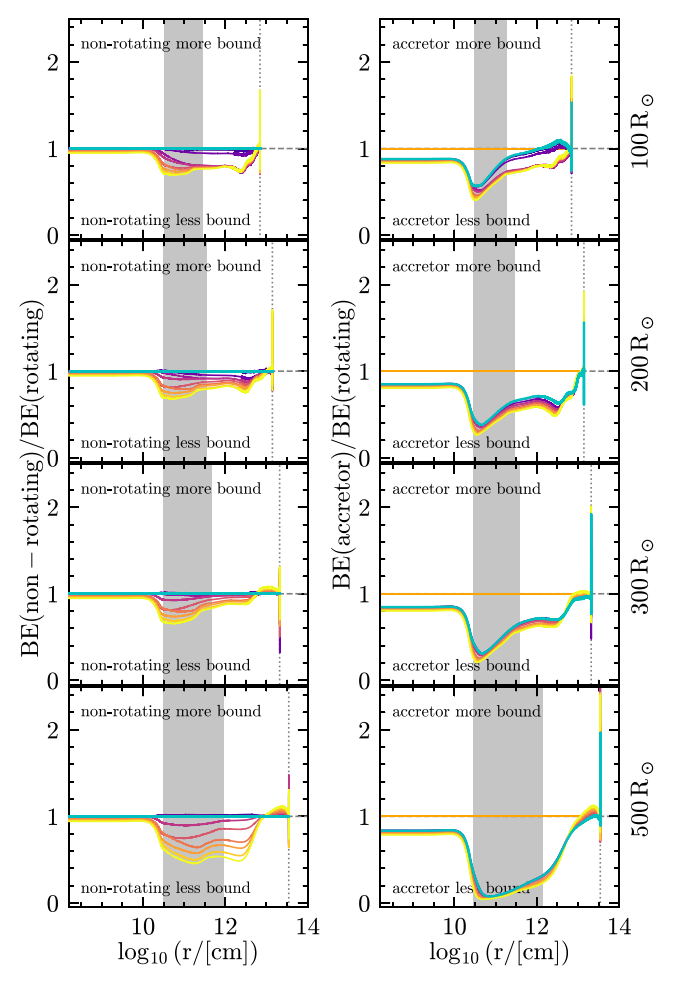


Figure 8. Ratio of binding energy of a nonrotating $18 M_{\odot}$ model (left) or of our $15 \rightarrow 18 M_{\odot}$ accretor (right) divided by the binding energy of the rotating models of Figure 7. The binding energy includes the internal energy ($\alpha_{\rm th} = 1$); the gray bands highlight the CEB region of the models in the numerator. Lighter colors indicate ratios to an initially faster-rotating single star; see also legend in Figure 7.

although the timing and amplitude of the impact of mixing and rotation can be different than for single stars (e.g., Renzo & Gotberg 2021). Future work should investigate how to include the effect in rapid population synthesis, for example with a prescription for λ_{CE} (see Appendix D).

Appendix B Binding Energy Profiles

In Figure 9, we show the binding energy of our accretor models (solid lines, including the internal energy, i.e., $\alpha_{th} = 1$

in Equation (1)); single stars with initial mass roughly equal to the corresponding accretor's post-RLOF mass, and our engineered models (see also Figure 11 for the $\lambda_{\rm CE}$ profile defined in Appendix D). The two lowest mass accretors (left and central column) do not expand to $R=1000\,R_\odot$ before carbon depletion. Generally speaking, the accretors (orange) have lower binding energies than corresponding single stars (red), and their profiles are qualitatively closer to the engineered models with the steepest core (darker curves), although local deviations from this trend can occur for some r.

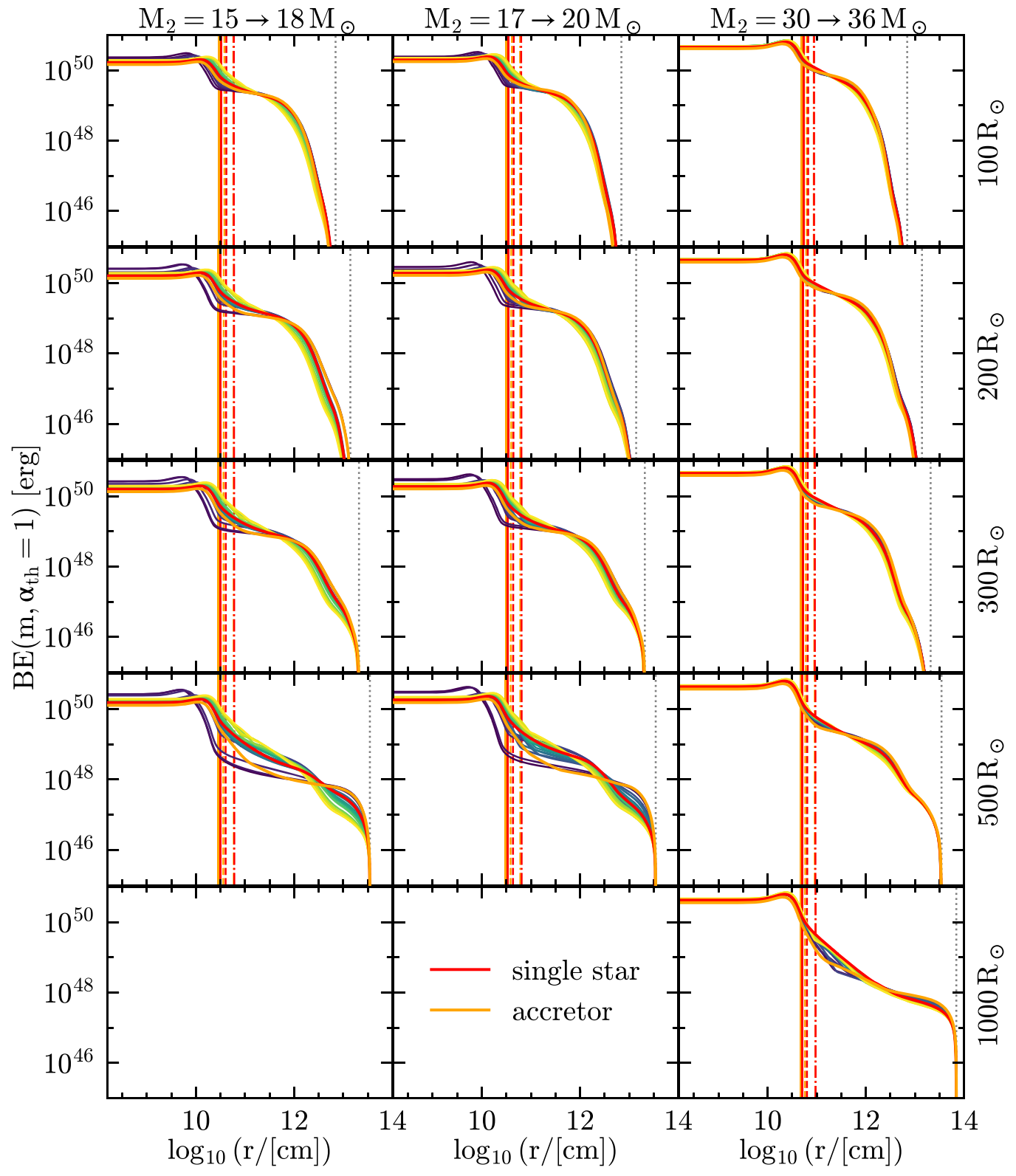


Figure 9. Binding energy profile at fixed photospheric radius R (right y-axis) as a function of radial coordinate r. We only show profiles with $\alpha_{th} = 1$, which is accounting for the internal energy content of the star. Orange, red, and other colors show, respectively, the accretor models, single stars of same post-RLOF total mass, and engineered models with varying CEB steepness (increasing CEB size from blue to yellow; see Figure 2). Titles indicates the pre-RLOF and approximate post-RLOF accretor masses. The vertical colored lines mark the outer edge of the helium cores of the accretor and single star, which is the outermost location where Y > 0.1 and X < 0.01 (solid lines), or X < 0.1 (dashed), or X < 0.2 (dotted-dashed). The dotted gray lines mark the total radius R of these models.

Appendix C Comparison with Same Core Mass

Figure 2 compares our accretor models to stars of the same total post-RLOF mass. However, it is not obvious that models of the same total mass are the most relevant comparison: for instance, the (helium or carbon–oxygen) core mass is often used to determine the final compact object

(e.g., Fryer et al. 2012, 2022; Farmer et al. 2019; Patton & Sukhbold 2020; Renzo et al. 2022), and comparing models of roughly the same core mass might be more appropriate (but is sensitive to the condition defining the core edge). We show in Figure 10 a comparison of our accretors with models of the same total *initial* mass, which constitute the extreme opposite comparison point.

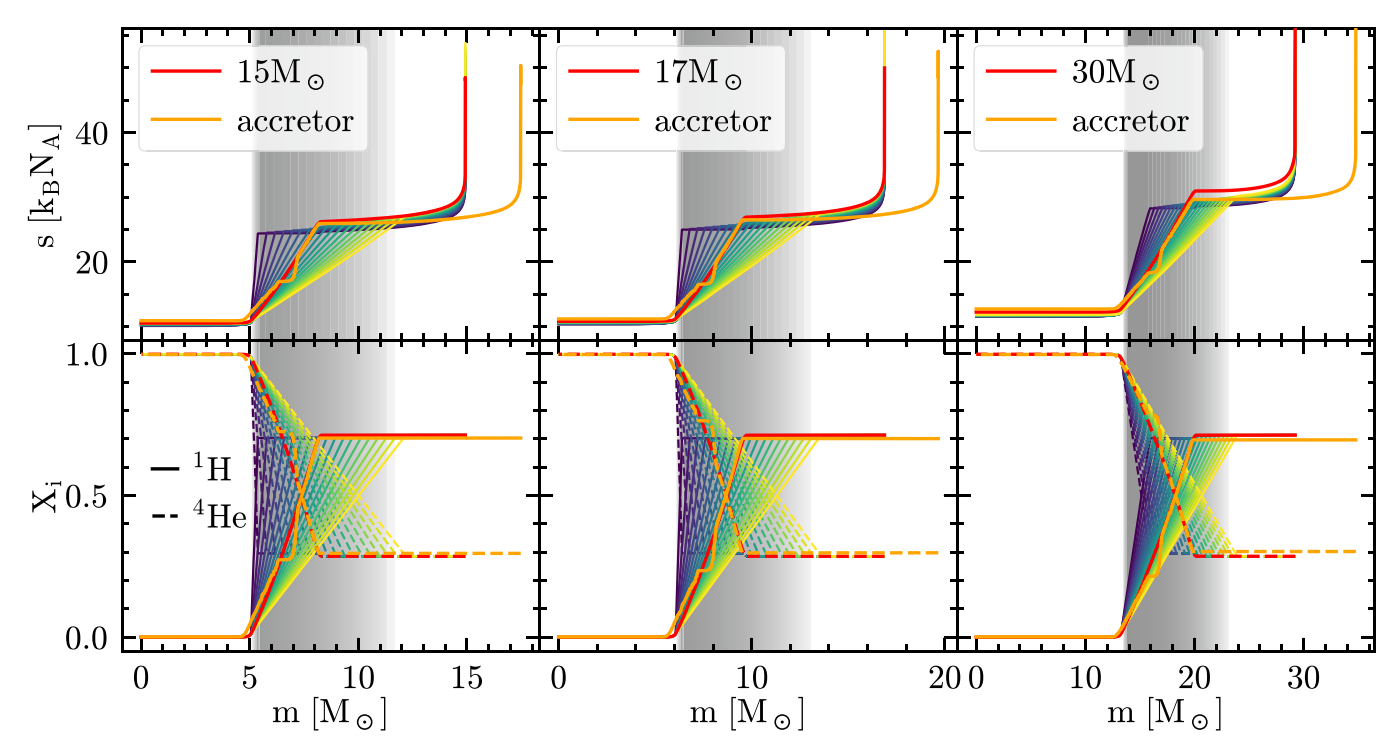


Figure 10. Specific entropy (top row), H (bottom row, solid lines), and He (bottom row, dashed lines) profiles for nonrotating single stars (red), accretors (orange), and "engineered" models of the same total mass as the ZAMS mass of the accretors. The overlapping gray bands emphasize the CEB region, increasing in size from blue to yellow in the engineered models.

Appendix D Common Envelope λ_{CE}

De Kool (1990) introduced a binding energy parameter $\lambda_{\rm CE}$ to account for the internal structure of the stars when

calculating the post-CE orbit using energy conservation:

$$\lambda_{\rm CE} \equiv \lambda_{\rm CE}(m) = \left(GM(M-m)/R \right) / BE(m, \, \alpha_{\rm th} = 1.0) \,, \tag{3}$$

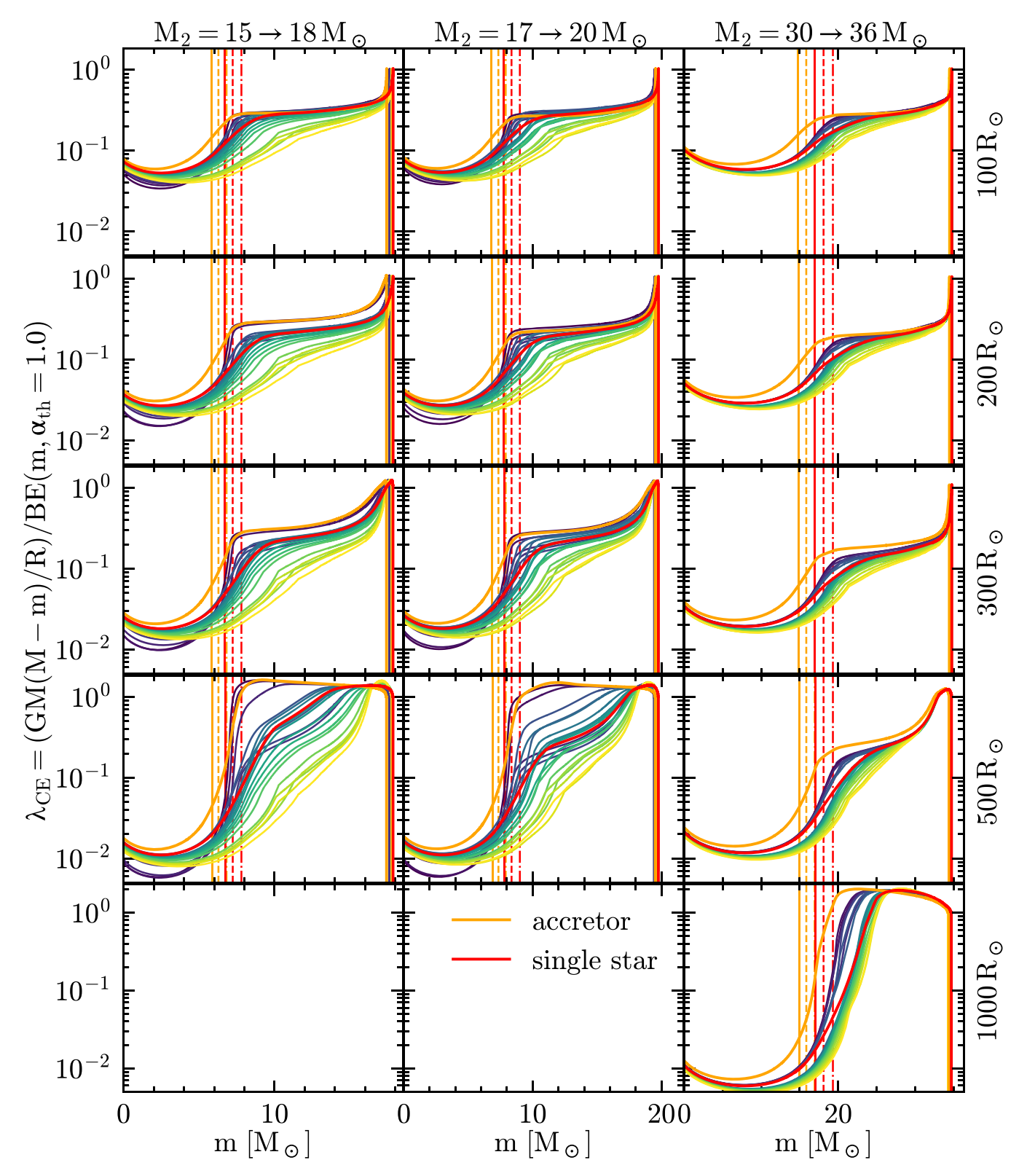


Figure 11. Profile of the binding energy parameter λ_{CE} as a function of mass coordinate for accretors (orange), single stars (red), and our engineered stars (other colors) at selected total radii. The vertical lines mark the outer edge of the helium cores of the accretor and single star, which is the outermost location where Y > 0.1 and X < 0.01 (solid lines), or X < 0.1 (dashed), or X < 0.2 (dotted-dashed). The CEB size of engineered models increases from blue to yellow.

where again the Lagrangian mass coordinate m can be interpreted as a variable core mass (see also De Marco et al. 2011; Ivanova et al. 2013). While de Kool (1990) implicitly used $\alpha_{\rm th}=0$, we calculate $\lambda_{\rm CE}$ with $\alpha_{\rm th}=1.0$ (including recombination energy), which provides a best case scenario for the ejection of the CE by harvesting the entire internal energy available in the gas. We show in Figure 11 the $\lambda_{\rm CE}$ profiles for our models.

Appendix E Reproducibility

This study was carried out using the reproducibility software **show your work!** (Luger et al. 2021), which leverages continuous integration to programmatically download the data from zenodo.org, create the figures, and compile the manuscript. Each figure caption contains two links: one to the data set stored on zenodo used in the corresponding figure, and the other to the script used to make the figure (at the commit corresponding to the current build of the manuscript). The git repository associated to this study is publicly available at https://github.com/mathren/CE_accretors, and the release v.2.1 allows anyone to rebuild the entire manuscript. The data sets are stored at doi:10.5281/zenodo. 7343715, including the template setup to recreate them using MESA (version 15140 and the software development kit x86_64-linux-20.12.1) and the scripts used to produce the figures.

ORCID iDs

```
M. Renzo  https://orcid.org/0000-0002-6718-9472
E. Zapartas  https://orcid.org/0000-0002-7464-498X
S. Justham  https://orcid.org/0000-0001-7969-1569
K. Breivik  https://orcid.org/0000-0001-5228-6598
M. Lau  https://orcid.org/0000-0002-6592-2036
R. Farmer  https://orcid.org/0000-0003-3441-7624
M. Cantiello  https://orcid.org/0000-0002-8171-8596
B. D. Metzger  https://orcid.org/0000-0002-4670-7509
```

References

```
Anders, E. H., Jermyn, A. S., Lecoanet, D., & Brown, B. P. 2022a, ApJ,
Anders, E. H., Jermyn, A. S., Lecoanet, D., et al. 2022b, ApJL, 928, L10
Andrews, J. J., Breivik, K., & Chatterjee, S. 2019, ApJ, 886, 68
Belczynski, K., Holz, D. E., Bulik, T., & O'Shaughnessy, R. 2016, Natur,
  534, 512
Blaauw, A. 1961, BAN, 15, 265
Blaauw, A. 1993, in ASP Conf. Ser. 35, Massive Stars: Their Lives in the
   Interstellar Medium, ed. J. P. Cassinelli & E. B. Churchwell (San Francisco,
Blagorodnova, A., Klencki, N., Pejcha, O., et al. 2021, A&A, 653, A134
Brandt, N., & Podsiadlowski, P. 1995, MNRAS, 274, 461
Braun, H., & Langer, N. 1995, A&A, 297, 483
Breivik, K., Chatterjee, S., & Larson, S. L. 2017, ApJL, 850, L13
Breivik, K., Coughlin, S., Zevin, M., et al. 2020, ApJ, 898, 71
Broekgaarden, F. S., & Berger, E. 2021, ApJL, 920, L13
Brott, I., de Mink, S. E., Cantiello, M., et al. 2011, A&A, 530, A115
Cantiello, M., Yoon, S., Langer, N., & Livio, M. 2007, A&A, 465, L29
Chawla, C., Chatterjee, S., Breivik, K., et al. 2022, ApJ, 931, 107
Claret, A., & Torres, G. 2017, ApJ, 849, 18
de Kool, M. 1990, ApJ, 358, 189
De Marco, O., Passy, J.-C., Moe, M., et al. 2011, MNRAS, 411, 2277
de Mink, S. E., & Mandel, I. 2016, MNRAS, 460, 3545
Delgado, A. J., & Thomas, H. C. 1981, A&A, 96, 142
Dewi, J. D. M., & Tauris, T. M. 2000, A&A, 360, 1043
```

Dominik, M., Belczynski, K., Fryer, C., et al. 2012, ApJ, 759, 52

```
Eggleton, P. P. 1983, ApJ, 268, 368
El-Badry, K., Seeburger, R., Jayasinghe, T., et al. 2022, MNRAS, 512, 5620
Farmer, R., & Bauer, E. B. 2018, Rjfarmer/Pymesa: Add Support For
   10398, v1.0.3, Zenodo, doi:10.5281/zenodo.1205271,
Farmer, R., Fields, C. E., Petermann, I., et al. 2016, ApJS, 227, 22
Farmer, R., Renzo, M., de Mink, S. E., Marchant, P., & Justham, S. 2019, ApJ,
Farrell, E., Groh, J. H., Meynet, G., & Eldridge, J. J. 2022, MNRAS, 512, 4116
Fragos, T., Andrews, J. J., Bavera, S. S., et al. 2022, arXiv:2202.05892
Fryer, C. L., Belczynski, K., Wiktorowicz, G., et al. 2012, ApJ, 749, 91
Fryer, C. L., Olejak, A., & Belczynski, K. 2022, ApJ, 931, 94
Gagnier, D., Rieutord, M., Charbonnel, C., Putigny, B., & Espinosa Lara, F.
   2019, A&A, 625, 1
Gotberg, Y., de Mink, S. E., Groh, J. H., et al. 2018, A&A, 615, A78
Han, Z., Podsiadlowski, P., & Eggleton, P. P. 1995, MNRAS, 272, 800
Heger, A., Langer, N., & Woosley, S. E. 2000, ApJ, 528, 368
Hellings, P. 1983, Ap&SS, 96, 37
Hellings, P. 1984, Ap&SS, 104, 83
Hirai, R., Podsiadlowski, P., & Yamada, S. 2018, ApJ, 864, 119
Hjellming, M. S., & Webbnik, R. F. 1987, ApJ, 318, 794
Hunter, J. D. 2007, CSE, 9, 90
Hurley, J. R., Tout, C. A., & Pols, O. R. 2002, MNRAS, 329, 897
Ivanova, N., Justham, S., Chen, X., et al. 2013, A&ARv, 21, 59
Ivanova, N., Justham, S., & Ricker, P. 2020, AAS-IOP Astronomy Book Series
   (Bristol: IOP Publishing), 2514
Jermyn, A. S., Bauer, E. B., Schwab, J., et al. 2022, arXiv:2208.03651
Kalogera, V. 1996, ApJ, 471, 352
Kippenhahn, R., & Weigert, A. 1967, ZA, 65, 251
Klencki, J., Istrate, A., Nelemans, G., & Pols, O. 2022, A&A, 662, A56
Klencki, J., Nelemans, G., Istrate, A. G., & Chruslinska, M. 2021, A&A,
   645, A54
Kruckow, M. U., Tauris, T. M., Langer, N., Kramer, M., & Izzard, R. G. 2018,
   MNRAS, 481, 1908
Langer, N. 1998, A&A, 329, 551
Laplace, E., Gotberg, Y., de Mink, S. E., Justham, S., & Farmer, R. 2020,
     &A, 637, A6
Laplace, E., Justham, S., Renzo, M., et al. 2021, A&A, 656, A58
Lau, M. Y. M., Hirai, R., González-Bolívar, M., et al. 2022a, MNRAS,
Lau, M. Y. M., Hirai, R., Price, D. J., & Mandel, I. 2022b, MNRAS, 516, 4669
Law-Smith, J. A. P., Everson, R. W., Ramirez-Ruiz, E., et al. 2020,
   arXiv:2011.06630
Lubow, S. H., & Shu, F. H. 1975, ApJ, 198, 383
Luger, R., Bedell, M., Foreman-Mackey, D., et al. 2021, arXiv:2110.06271
Luger, R., Foreman-Mackey, D., & Hedges, C. 2021, AJ, 162, 124
Maeder, A., & Meynet, G. 2000, ARA&A, 38, 143
Marchant, P., Pappas, K. M. W., Gallegos-Garcia, M., et al. 2021, A&A,
   650, A107
Moravveji, E., Townsend, R. H. D., Aerts, C., & Mathis, S. 2016, ApJ,
   823, 130
Morton, D. C. 1960, ApJ, 132, 146
Muller, P. E., & Vink, J. S. 2014, A&A, 564, 1
Nandez, J. L. A., Ivanova, N., & Lombardi, J. C., Jr. 2014, ApJ, 786, 39
Neo, S., Miyaji, S., Nomoto, K., & Sugimoto, D. 1977, PASJ, 29, 249
O'Connor, E., & Ott, C. D. 2011, ApJ, 730, 70
Ogata, M., Hirai, R., & Hijikawa, K. 2021, MNRAS, 505, 2485
Packet, W. 1981, A&A, 123, 7254
Paczynski, B. 1971, ARA&A, 9, 183
Paczynski, B. 1976, in IAU Symp. 73, Structure and Evolution of Close Binary
   Systems, ed. P. Eggleton, S. Mitton, & J. Whelan (Dordrecht: Reidel), 75
Patton, R. A., & Sukhbold, T. 2020, MNRAS, 499, 2803
Patton, R. A., Sukhbold, T., & Eldridge, J. J. 2022, MNRAS, 511, 903
Pavlovskii, K., Ivanova, N., Belczynski, K., & Van, K. X. 2017, MNRAS,
Paxton, B., Bildsten, L., Dotter, A., et al. 2011, ApJS, 192, 3
Paxton, B., Cantiello, M., Arras, P., et al. 2013, ApJS, 208, 4
Paxton, B., Marchant, P., Schwab, J., et al. 2015, ApJS, 220, 15
Paxton, B., Schwab, J., Bauer, E. B., et al. 2018, ApJS, 234, 34
Paxton, B., Smolec, R., Schwab, J., et al. 2019, ApJS, 243, 10
Pejcha, O., Metzger, B. D., Tyles, J. G., & Tomida, K. 2017, ApJ, 850, 59
Perez, F., & Granger, B. E. 2007, CSE, 9, 21
Ramirez-Agudelo, O. H., Sana, H., de Mink, S. E., et al. 2015, A&A, 580, A92
Renzo, M., Farmer, R. J., Justham, S., Mink, S. E. D., & Marchant, P. 2020,
   MNRAS, 4341, 4333
```

DornWallenstein, T. Z., Levesque, E. M., Neugent, K. F., et al. 2020, ApJ,

902, 24

```
Renzo, M., Callister, T., Chatziioannou, K., et al. 2021, ApJ, 919, 128
Renzo, M., & Gotberg, Y. 2021, ApJ, 923, 277
Renzo, M., Hendriks, D. D., van Son, L. A. C., & Farmer, R. 2022, RNAAS, 6, 25
Renzo, M., Ott, C., Shore, S., & De Mink, S. 2017, A&A, 603, A118
Renzo, M., Zapartas, E., de Mink, S. E., et al. 2019, A&A, 624, A66
Sen, K., Langer, N., Marchant, P., et al. 2022, A&A, 659, A98
Sravan, N., Marchant, P., & Kalogera, V. 2019, ApJ, 885, 130
Tauris, T. M., & Dewi, J. D. M. 2001, A&A, 369, 170
Tauris, T. M., Kramer, M., Freire, P. C. C., et al. 2017, ApJ, 846, 170
Tauris, T. M. M., & Takens, R. J. J. 1998, A&A, 1059, 1047
Tutukov, A. V., & YungelSon, L. R. 1993, MNRAS, 260, 675
van den Heuvel, E. P. J., Portegies Zwart, S. F., & de Mink, S. E. 2017, MNRAS, 471, 4256
```

van der Walt, S., Colbert, S. C., & Varoquaux, G. 2011, CSE, 13, 22 van Son, L. A. C., de Mink, S. E., Callister, T., et al. 2022, ApJ, 931, 17 Vigna-Gomez, A., MacLeod, M., Neijssel, C. J., et al. 2020, PASA, 37, e038 Vigna-Gomez, A., Neijssel, C. J., Stevenson, S., et al. 2018, MNRAS, 481, 4009 Virtanen, P., Gommers, R., Oliphant, T. E., et al. 2020, NatMe, 17, 261 Walmswell, J. J., Tout, C. A., & Eldridge, J. J. 2015, MNRAS, 447, 2951 Wang, C., Langer, N., Schootemeijer, A., et al. 2020, ApJL, 888, L12 Wang, L., Gies, D. R., Peters, G. J., et al. 2021, AJ, 161, 248 Webbink, R. F. 1984, ApJ, 277, 355 Yoon, S. C., & Langer, N. 2005, A&A, 443, 643 Zapartas, E., de Mink, S. E., Izzard, R. G., et al. 2017, A&A, 601, A29 Zapartas, E., Renzo, M., Fragos, T., et al. 2017, A&A, 656, L19 Zorotovic, M., Schreiber, M. R., Gansicke, B. T., & Nebot Gomez-Moran, A. 2010, A&A, 520, A86